Journal of Metals, Materials and Minerals, 35(2), e2220, 2025

Influence of the casting processes and aging times on the microstructure and hardness of AlSi$_{12}$Cu cast alloys

Said BEROUAL[1,*], Pascal PAILLARD[2], and Yann BORJON-PIRON[2]

[1] *University of Oum El Bouaghi/ Department of Mechanical Engineering, LACM, Oum El Bouaghi, 04000, BP 358, Algeria*
[2] *Institute of Materials Jean Rouxel, IMN–ID2M, UMR 6502, Nantes 44306, BP 50609, France*

***Corresponding author e-mail**: said.beroual@univ-oeb.dz

Received date:
5 December 2024
Revised date:
4 April 2025
Accepted date:
22 April 2025

Keywords:
AlSi$_{12}$Cu alloys;
Microstructure;
Aging;
Precipitation;
Hardness

Abstract

The present study investigated the effects of the casting processes and aging times on the microstructure and hardness of commercial AlSi$_{12}$Cu alloys. The primary goal was to assess how various aging times affect the maximum hardness of the alloy and to evaluate the influence of cooling rates on hardness values obtained from sand casting (SC) and High-pressure die casting (HPDC). For both casting alloys, the solution heat treatment was performed at 540°C, followed by quenching. The alloys were then aged at 180°C for various durations, ranging from 10 min to 50 h. The results reveal significant microstructural changes in the size and morphology of the eutectic silicon and intermetallic phases between the SC and HPDC. The α-Fe intermetallics predominantly exhibit a Chinese-script morphology in SC, whereas in HPDC, they are primarily present as polyhedral particles. The maximum hardness peak was observed at 8 h of aging in SC; in HPDC, it was achieved at only 4 h of aging. The results of the hardness and X-ray diffraction (XRD) analyses exhibit consistent trends, strong alignment, and good agreement with each other. The HPDC process, combined with heat treatment, significantly enhances the mechanical properties of cast aluminum alloys.

1. Introduction

Cast aluminum–silicon alloys are widely used in the automotive industry because of their good casting characteristics and mechanical properties. In addition to their high strength-to-weight ratio, they exhibit excellent resistance to abrasion and corrosion, a low coefficient of thermal expansion, and good weldability [1-3]. However, the microstructural constituents of their structure influence the mechanical properties of these alloys after casting through the size of the α-Al dendrites, morphology and quantity of intermetallic phases. In sand casting (SC), Al-Si alloys readily exhibit eutectic silicon in acicular or lamellar forms, resulting in a concentration of stress, and therefore tend to exhibit low strength and ductility [3,4]. To produce components exposed to harsh service conditions, HPDC is used to create high-strength parts with excellent surface finish characteristics.

The high pressures and rapid solidification rates of this process produce a refined microstructure, which includes silicon eutectics and intermetallics [5]. Several studies have demonstrated that increased cooling rates significantly modify the eutectic structure, resulting in a more refined microstructure. In HPDC, this refinement is primarily attributed to higher cooling rates, shorter solidification times, and applied pressure. The use of metal molds with high thermal conductivity facilitates rapid heat extraction, thereby limiting grain growth and phase coarsening. Conversely, the slower cooling and lack of pressure in SC lead to larger, coarser grains. This refined microstructure enhances the alloy's mechanical properties [6-8].

The mechanical properties of aluminum–silicon alloys are influenced not only by the morphology of the α–Al dendrites, silicon particle size, and intermetallic phases but also by the chemical composition of these alloys. The introduction of alloying elements such as copper (Cu) and/or magnesium (Mg) induces the formation of hardening phases, which strengthen the alloy during the heat treatment process [9,10].

Iron is a significant impurity in commercial Al-Si alloys, adversely affecting their mechanical properties. However, adding 0.7 wt% iron to cast aluminum alloys is common to prevent soldering and sticking to the die [11]. In Al-Si alloys, iron typically forms β-Al$_5$FeSi (β-Fe) platelets. When combined with manganese and chromium, it forms α-Al$_{15}$(FeMnCr)$_3$Si$_2$ (α-Fe) sculptures that resemble Chinese-script. However, if the combined manganese and iron content exceeds 0.8 wt%, α-Fe crystals become primary, appearing as polyhedral particles known as sludge [12]. In industrial Al-Si-Cu-Mg alloys with added Fe, Mn, and Cr, the abovementioned phases can coexist in various forms depending on the solidification rate [3,13].

The effects of the copper and magnesium contents on microstructure and hardness have been widely studied, demonstrating that appropriate levels of these elements enhance the mechanical properties of alloys. For example, Kori *et al.* [14] reported that minor additions of 0.5 wt% copper and 0.7 wt% magnesium significantly enhanced the mechanical properties of A356 alloys. Shabestari *et al.* [9] studied Al-Si-Mg alloys with varying copper contents (0.2 wt% to 2.5 wt%) and reported that alloys cast in graphite molds with approximately 1.5 wt% copper exhibited the best mechanical properties. Alfonso *et al.* [15] reported that for magnesium contents of up to 6.78 wt% in aluminum alloys, the hardness increased with increasing magnesium concentration. This effect is attributed to the strengthening influence of magnesium, which enhances precipitation hardening and contributes to the development of a more refined and robust microstructure. Taylor *et al.* [16] investigated the effect of the addition of Mg to aluminum alloys and reported that Mg concentrations between 0.3 wt% and 0.7 wt% facilitated the formation of Mg_2Si. They reported that the yield strength increased significantly at approximately 0.4 wt% Mg. However, when the Mg concentration exceeded 0.5 wt%, the yield strength began to decrease. However, Samuel *et al.* [10] reported that magnesium content has no significant effect on hardness when it exceeds 0.3 wt%.

The solution process is carried out to produce a supersaturated solid solution that dissolves phases such as β-Mg_2Si, θ-Al_2Cu, Q-$Al_5Cu_2Mg_8Si$, and π-Al_8FeMg_3Si in the alloy structure. However, the solution temperature is limited by the melting temperature of the eutectic phase. Mondolfo [12] reported that low melting point eutectics control solution temperatures, which are generally below 830 K (557°C) for copper-free alloys and below 810 K (537°C) for copper-rich alloys. Shivkumar *et al.* [17] reported that the solution temperature during alloy processing is influenced by the composition of the alloy, particularly the copper and iron contents. They reported that increasing the solution temperature reduces the solution time and improves the strength properties of Al-Si-Mg alloys up to 550°C. However, above 560°C, the formation of the first liquid phase begins at the grain boundaries. Samushina *et al.* [18] reported that, in an $AlSi_{12}Cu_2MgNi$ alloy with 1.7 wt% Cu heat-treated at 540°C, there were clear signs of overburning, whereas this phenomenon was not detected in the 1 wt% Cu alloy structure.

The final step in determining the properties of heat-treated aluminum alloys is the aging time (T6). After the supersaturated solid solution is maintained at a relatively high temperature, followed by rapid water quenching, the return to equilibrium can be accelerated by aging precipitation. Although precipitation reactions in ternary Al-Si-Cu and Al-Si-Mg alloys have been widely studied, the precipitation sequence in quaternary Al-Si-Cu-Mg alloys is not fully understood, as noted by Sjölander *et al.* [19]. According to Ouellet *et al.* [20], the hardening process during aging in Al-Si-Cu-Mg alloys takes place through the cooperative precipitation of θ-Al_2Cu and β-Mg_2Si hardening particles. Li *et al.* [21] reported that a double aging peak was present in the age hardening curve for the Al-Si-Cu-Mg alloy, whereas in the curves for the Al-Si-Mg and Al-Si-Cu alloys, a single aging peak was observed. A recent study by Dong *et al.* [22] on $Al_9Si_{0.5}Mg_xCu$ alloys solution-treated at 540°C for 8 h with aging at 190°C revealed that the hardness and yield strength reached maximum values when the copper composition was between 0.4% and 0.85% by weight. Further increases in copper content beyond this range were not beneficial for industrial applications, as they only led to a reduction in ductility.

The alloy investigated in this study is a cast $AlSi_{12}Cu$ alloy, which is classified as 413.0 by the Aluminum Association and EN AC 47000 in the European standard [1,23]. These alloys have a "eutectic" composition and are characterized by high fluidity. They are used in applications requiring increased corrosion resistance and high-definition surfaces.

This study investigated the microstructure and hardness evolution of a commercial $AlSi_{12}Cu$ alloy obtained through both sand casting and high-pressure die-casting followed by T6 aging treatment. All heat-treated samples underwent hardness testing and XRD analyses. The morphologies of the intermetallic phases in the alloy were observed using optical and Scanning electron microscopy (SEM) both in the as-cast state and after heat treatment. The alloy phases were further analyzed and identified through energy-dispersive X-ray spectroscopy (EDS). The results are compared and discussed below.

2. Experimental

The $AlSi_{12}Cu$ alloy used in this research was supplied as a commercial ingot. The chemical composition of the ingot was determined and is shown in Table 1. The alloy was heated to 800°C and subsequently maintained at 720°C. The melt was poured manually (i) by conventional gravity into a sand mold SC and (ii) into a die-casting machine HPDC. The molten metal in the HPDC was poured into a cold chamber, and the piston rod was hydraulically pushed forward to fill the die cavity. All the test samples used in this study were taken from castings of the same cross-section (approximately 1 cm × 2.5 cm). According to the ASM Handbook committee [1], the average cooling rate in SCs typically falls within the range of $0.1°C\cdot s^{-1}$ to $0.5°C\cdot s^{-1}$. However, in the case of HPDC, the cooling rates are even higher, ranging from $50°C\cdot s^{-1}$ to $500°C\cdot s^{-1}$.

Castings obtained by the two molding processes, SC and HPDC, were subjected to T6 heat treatment. The solution must undergo sufficient heat treatment for an extended period to ensure effective diffusion. All the samples were subjected to solution heat treatment (SHT) at 540°C for 8 h. This choice was based on the results of previous research [18-20,23]. After undergoing the solution treatment, all the samples were quenched in water at 25°C, followed by aging at 180°C for various durations (10 min, 20 min, 40 min, 1 h, 2 h, 4 h, 8 h, 12 h, 20 h, 30 h, and 50 h).

The samples for metallurgical examination were cut from the as-cast alloy pieces that were prepared using both the SC and HPDC processes. All samples, both as-cast and heat-treated, were mounted and polished using an OP-U suspension and abrasive colloidal silica (0.4 µm). After polishing, the metallographic samples were etched with a H_2SO_4 (sulfuric acid) solution for 15 s. The etched samples were subsequently photographed using a Carl Zeiss optical microscope.

The intermetallic phases in the alloy were identified using a SEM (model ZEISS-Merlin) operating at 30 kV and 300 nA with a 1 mm radius electron beam. Chemical composition microanalysis was performed using an Oxford INCA EDS detector. Phase transformations during heat treatment were determined using XRD analyses conducted with a Bruker D8 Advance diffractometer, LynxEye detector, and Cu Ka

Table 1. Chemical composition of the commercial $AlSi_{12}Cu$ alloy (wt%).

Al	Si	Cu	Fe	Mg	Mn	Cr	Zn	Ti	Pb	Sn
Balance	10.65	0.80	0.75	0.23	0.16	0.01	0.08	0.04	0.02	0.004

radiation (40 kV/40 mA) in the 2θ range from 20° to 120°. Some samples were deeply etched using a reagent composed of 66% HCl, 33% HNO_3, and 1% HF to reveal the three-dimensional morphologies of the intermetallic phases. The residual deposits from the etching process were removed by rinsing with alcohol.

Vickers hardness measurements were conducted using a DuraScan 70 Durometer. All the as-cast samples subjected to both solution heat treatment and aging for both casting processes underwent an HV5 test with an applied load of 49.2 N, which was maintained for nearly 10 s. The average hardness values from the fifteen readings, along with their respective error bars, were evaluated.

3. Results and discussion

3.1 As-cast microstructures

In all commercial processes, solidification takes place through the formation of dendrites in the liquid solution. During solidification, inclusions and eutectic silicon can segregate into the spaces between the arms of the dendrites. Figure 1 shows the microstructures of the $AlSi_{12}Cu$ alloy obtained from the SC and HPDC processes. Both microstructures consisted of primary aluminum (α-Al) dendrites surrounded by eutectic silicon (Si) and various intermetallic phases. In SC, as shown in Figure 1(a), a prolonged solidification time resulted in a coarser microstructure with a large secondary dendrite arm spacing (SDAS) and coarse Si eutectic platelets. The average SDAS of the microstructures was approximately 30 µm, as determined through more than 10 measurements. Figure 1(b) shows the refinement of the Si eutectic phase during HPDC, along with the irregular morphology of the α-Al dendrites. This morphology is attributed to the formation of externally solidified crystals (ESCs) within the shot sleeve. Solidification initiates as the metal flows through the shot sleeve and contacts the cold chamber wall. ESCs containing liquid are injected into the die cavity at a high cooling rate under the high pressure exerted by the machine's clamping force. Consequently, the alloy undergoes multiple stages of deformation, where flow and solidification behaviors are coupled [24]. The precise measurement of the temperatures during the SDAS in the HPDC process is challenging because of the nonuniform distribution of primary α-Al dendrites and thus cannot be calculated.

Figures 1(c-d) present Secondary electron scanning (SE) observations for SC and HPDC. In both microstructures, iron crystallizes as β-Fe platelets and as an α-Fe phase. The α-Fe phase appears in the SC as large Chinese-script structures, approximately 100 µm in size. In contrast, in HPDC, it manifests as primary polyhedral α-Fe particles (sludge), averaging 10 µm, which coexist with secondary proeutectic polyhedral α-Fe particles measuring less than 5 µm. This morphological difference is attributed to the higher cooling rate in HPDC, which prevents the polyhedral particles from transforming into Chinese-script structures due to the limited time available for such transformation [25]. β-Fe platelets can be categorized as primary (predendritic ~100 µm), preeutectic, coeutectic, or posteutectic (a few µm) depending on their size and growth duration from nucleation to final solidification in the alloy [26]. The curved β–Fe platelets, indicated by the green arrow in Figure 1(d), are found only in HPDC. This morphology is a result of the pressure applied by the clamping force during the final stages of solidification.

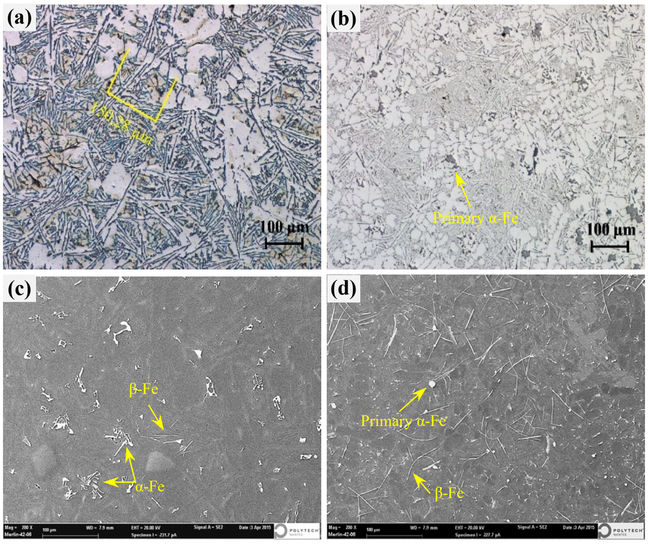

Figure 1. Micrographs of the $AlSi_{12}Cu$ alloys obtained from (a), (c) sand casting (SC) and (b), (d) high-pressure die casting (HPDC), (a-b) optical microscopy and (c-d) secondary electron (SE) images.

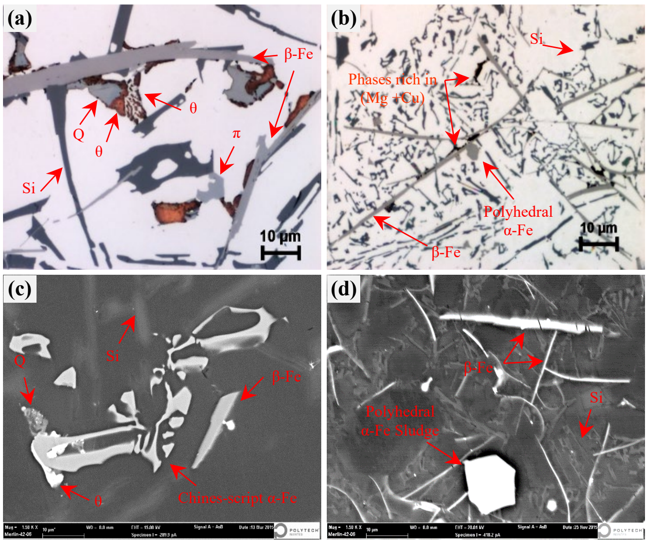

Figure 2. Micrographs of the $AlSi_{12}Cu$ alloy showing the main intermetallics observed: (a) and (c) in SC, (b) and (d) in HPDC; (a-b) optical microscopy and (c-d) backscattered electron images (BSE).

3.1.1 Micrographs of intermetallic phases

The SC alloy in Figure 2(a) has eutectic Si flakes and large intermetallic phases. In contrast, in Figure 2(b), the HPDC alloy shows a complete transformation of the eutectic Si morphology into a fine fibrous structure with smaller intermetallic phases. In the optical micrographs in Figure 2(a-b), the θ-Al_2Cu phase appears pink–brown, whereas the Q-$Al_5Cu_2Mg_8Si_6$ phase generally appears gray next to it. The eutectic Si displays a blue–gray color. Additionally, β-Fe platelets, α-Fe Chinese-script and α-Fe polyhedral particles generally appear light gray. The eutectic silicon particles measure up to approximately 200 µm in size due to the longer solidification time in SC, whereas in HPDC, they measure less than 10 µm. The conditions that influence the formation of α-Fe Chinese-script particles rather than α-Fe polyhedral particles are the cooling rate and the growth time required for the formation of these particles. In this alloy, the coexistence of all these particles has been observed in both casting processes, but with different quantities and sizes. The α-Fe Chinese-script structure is the most dominant structure in sand casting, as shown in Figure 1(c) and Figure 2(c), whereas polyhedral α-Fe particles are the predominant feature in the HPDC process, as shown in Figure 1(d) and Figure 2(d).

3.1.2 Phase identification with EDS analysis

The θ-Al_2Cu phases, shown in Figure 3(a), are approximately 30 µm in length, with this large size likely resulting from the slow cooling during SC. Copper can exist in two distinct forms: compact blocks or eutectic structures. However, the copper phases observed in the HPDC alloy in Figure 3(b) are very fine eutectic copper, with sizes no larger than 5 µm. These phases are typically observed growing on β-Fe platelets, which are considered favorable sites for their nucleation.

The Q-$Al_5Cu_2Mg_8Si_6$ phase, shown in Figure 2(a) and Figure 3(c), is commonly observed to grow simultaneously with the θ-Al_2Cu phase [27]. Owing to the low magnesium content (0.22 wt%), the presence of π-$Al_8Mg_3FeSi_6$ was rarely observed in this alloy. Once all the magnesium is consumed in the formation of the Q and π phases, the β-Mg_2Si phase becomes harder to detect. Seifeddine *et al.* [28] reported the rarity of Mg_2Si phases in an Al-Si-Cu-Mg alloy with a magnesium content of 0.4 wt%. The β-Mg_2Si phase in our alloy was identified as a dark black phase hollowed into the surface of the sample, as shown in Figure 3(c). Excess water during prolonged polishing and chemical etching reduces its surface to a level below that of the sample surface. In the HPDC alloy, the (Mg^+Cu)-rich phases shown in Figure 2(b) are difficult to identify by SEM because of their small size of approximately 1 µm.

Figure 4 presents analyses of the EDS spectra for the θ-Al_2Cu, Q-$Al_5Cu_2Mg_8Si_6$, β-Mg_2Si and π-$Al_8Mg_3FeSi_6$, β-Al_5FeSi and α-$Al_{15}(FeMnCr)_3Si_2$ phases observed during sand casting. The stoichiometry of the compact copper is very close to that of θ-Al_2Cu. The corresponding EDS spectrum, shown in Figure 4(a), indicates the presence of small amounts of Si and Fe. These minor concentrations of Si and Fe are attributed to the β-Fe platelets and Si eutectic surrounding this phase, potentially influencing analyses conducted using electron beam interactions. The spectra of the Q-$Al_5Cu_2Mg_8Si_6$, β-Mg_2Si, and π-$Al_8Mg_3FeSi_6$ phases reveal notably higher concentrations of Mg, which is consistent with their stoichiometric compositions, as shown in Figure 4(b) to Figure 4(d). The β-Fe platelets appear in both types of casting, but they can be up to 6 µm thick in SC, whereas they are only 2 µm thick in HPDC. This difference is attributed to the rapid and nonequilibrium cooling in HPDC. Figure 4(e) shows the EDS analysis of β-Fe platelets, revealing a stoichiometry that closely matches the typical β-Al_5FeSi phase. Cao *et al.* [26] reported that Fe-rich phases nucleate on the wet faces of double oxide films, while the space between the dry faces of the oxide films constitutes the cracks commonly observed in β-Fe platelets. This phenomenon was observed in both casting processes in this study. Figure 3(d) shows an example of β-Fe splitting in the HPDC. The α-Fe phase can exhibit various morphologies depending on factors such as the chemical composition, cooling rate, and solidification stage; it may appear as a star compound, a Chinese-script, or a polyhedral particle. The stoichiometry of this phase closely matches the primary $Al_{15}(FeMnCr)_3Si_2$ phase observed by Mondolfo [12], wherein iron, manganese, chromium, vanadium, and copper are all transition elements.

Figure 4(f) shows the α-Fe Chinese-script spectra in the SC, which are similar to those of the polyhedral α-Fe particles in the HPDC. Additionally, the EDS analysis spectra of small secondary proeutectic α-Fe particles in Figure 3(d) are identical to those of both Chinese-script and polyhedral particles.

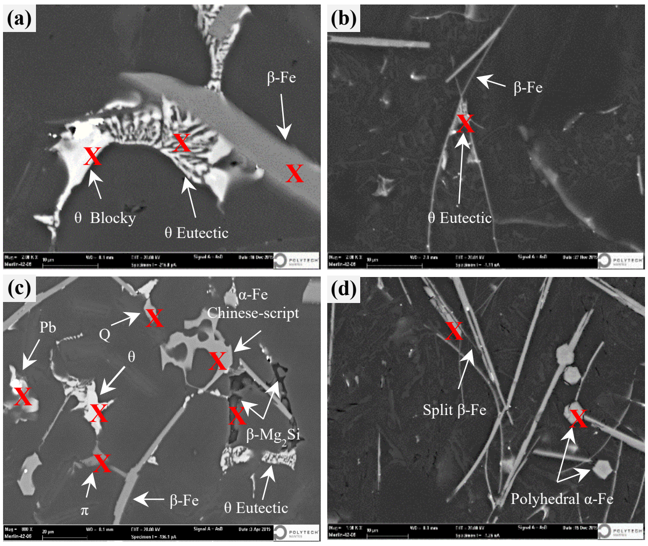

Figure 3. BSE micrographs of the $AlSi_{12}Cu$ alloy showing the main intermetallic phases in the SC (a), (c) and HPDC (b), (d).

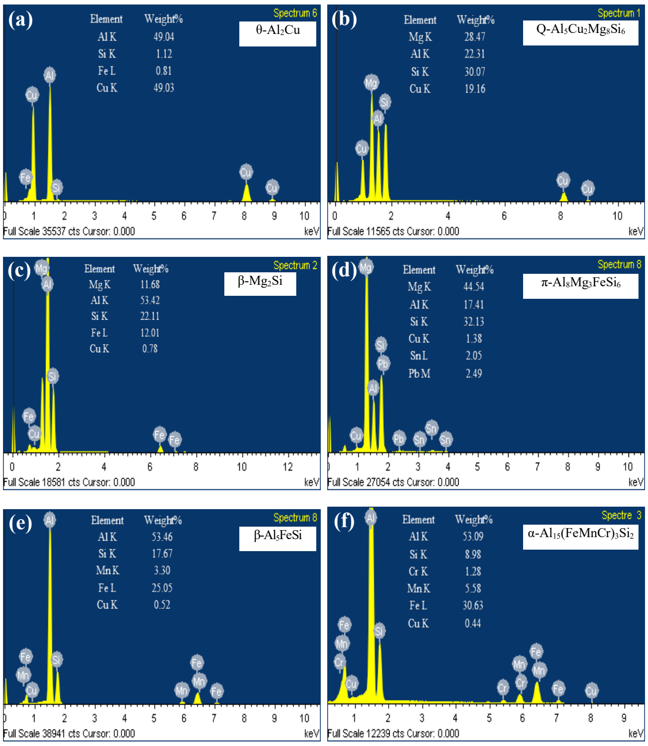

Figure 4. EDS spectra of phases in the as-cast $AlSi_{12}Cu$ alloy corresponding to (a) θ-Al_2Cu; (b) Q-$Al_5Cu_2Mg_8Si_6$; (c) π-$Al_8FeMg_3Si_6$; (d) β-Mg_2Si; (e) β-Al_5FeSi; and (f) α-$Al_{15}(FeMnCr)_3Si_2$.

3.1.3 Mapping analysis

The phases in HPDC are too fine to distinguish, so a single map is presented for SC. Figure 5 shows a BSE image surrounded by EDS maps of the elements Al, Si, Cu, Mg, Fe, Mn, and Cr. This figure shows the Chinese-script phases, a primary polyhedral α-Fe particle, β-Fe platelets, and the Q and θ phases. Chinese-script α-Fe phases are the predominant intermetallics in SC, whereas polyhedral α-Fe particles are rarely observed. As this figure shows, the polyhedral extends the arms and attempts to evolve into a Chinese-script morphology. This primary polyhedral α-Fe (approximately 25 µm) is likely formed at high temperatures during the predendritic stage of solidification [28].

The EDS maps reveal the presence of Mn in the polyhedral α-Fe particles and in the Chinese-script but not in the β-Fe platelets. The growth of this primary polyhedral α-Fe at elevated temperatures leads to the incorporation of some of the Cr present in the alloy, while simultaneously, the Chinese-script phase releases all the Cr into the matrix owing to the time required for its formation.

The EDS analysis of Fe, Cu, and Mg indicates that the Q-$Al_5Cu_2Mg_8Si_6$ phase is significantly enriched in Cu and Mg. In contrast, the π-$Al_8Mg_3FeSi_6$ phase is enriched primarily in Fe and Mg. These intermetallic phases form during the posteutectic reaction, occurring in the final stages of solidification.

3.2 Effect of solution heat treatment

After undergoing SHT at 540°C for 8 h, the θ-Al_2Cu and β-Mg_2Si, Q-$Al_5Cu_2Mg_8Si_6$ and π-$Al_8Mg_3FeSi_6$t phases completely dissolve, as shown in Figure 6. The microstructures observed through optical microscopy for SC and HPDC, as shown in Figure 6(a-b) respectively, illustrate the morphological changes in the silicon particles during SHT. The silicon particles became significantly coarser, adopted a more spherical shape and displayed increased spacing between them. According to our previous study (Beroual *et al.* [29]), the process begins with the fragmentation and spheroidization of eutectic silicon, followed by its subsequent coarsening. The β-Fe platelets and α-Fe Chinese-script phases also undergo dissolution and fragmentation. Tillova *et al.* [30] reported that during SHT at 505°C, the β-Fe platelets and α-Fe Chinese-script tend only toward fragmentation. However, with SHT at 525°C, fragmentation, segmentation, and dissolution tend to occur.

Figure 6(c-f) display the BSE images after SHT and aging for 4 h (c), 8 h (d), and 30 h (e-f). In these images, the β-Fe platelets, α-Fe Chinese-script structures, and polyhedral α-Fe particles appear to have dissolved and fragmented into fine particles, each smaller than 10 µm.

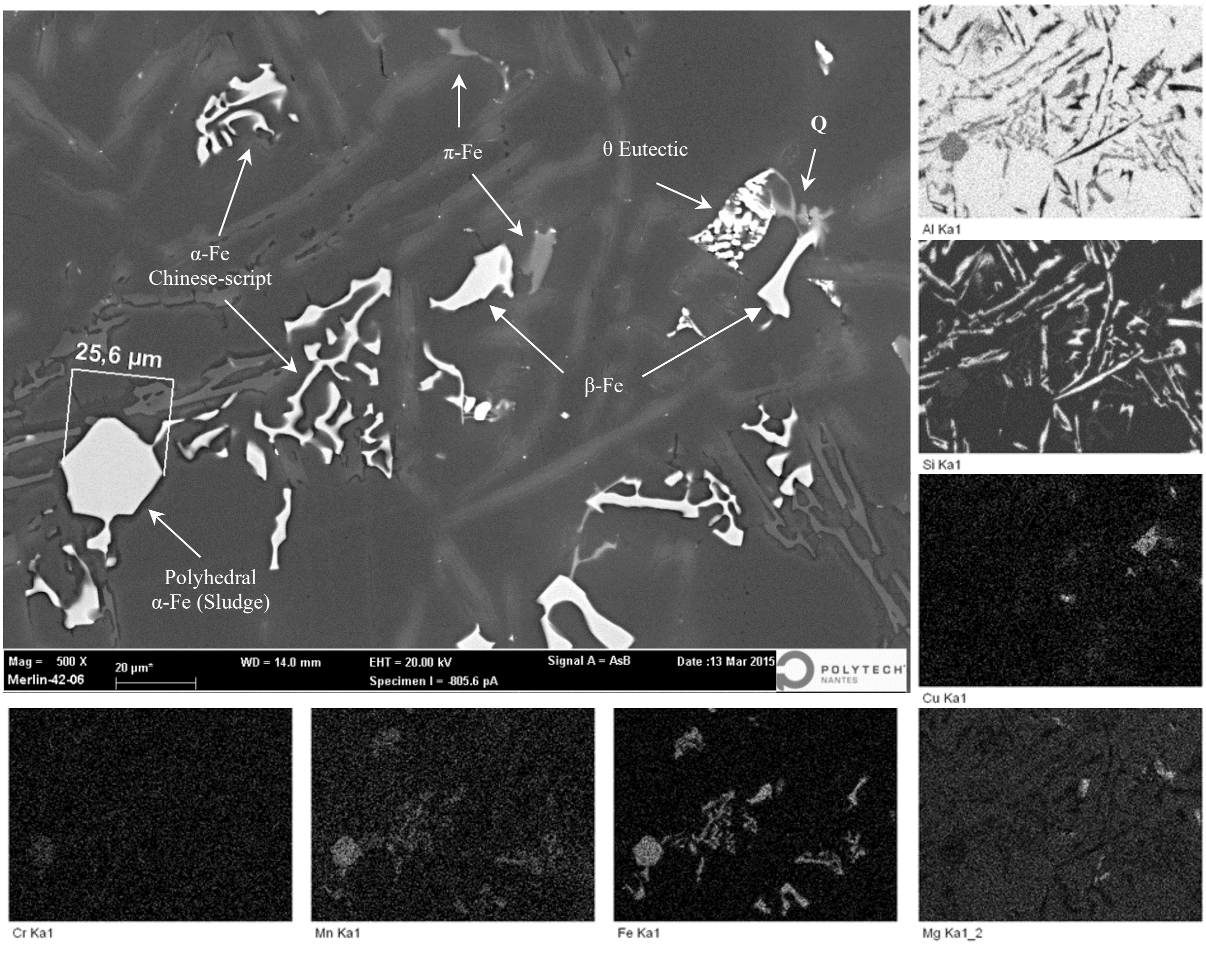

Figure 5. BSE image shows the morphologies of the α-Fe Chinese-script, α-Fe polyhedral, π, Q, and θ phases; and the corresponding EDS maps for the elements Al, Si, Cu, Mg, Fe, Mn, and Cr.

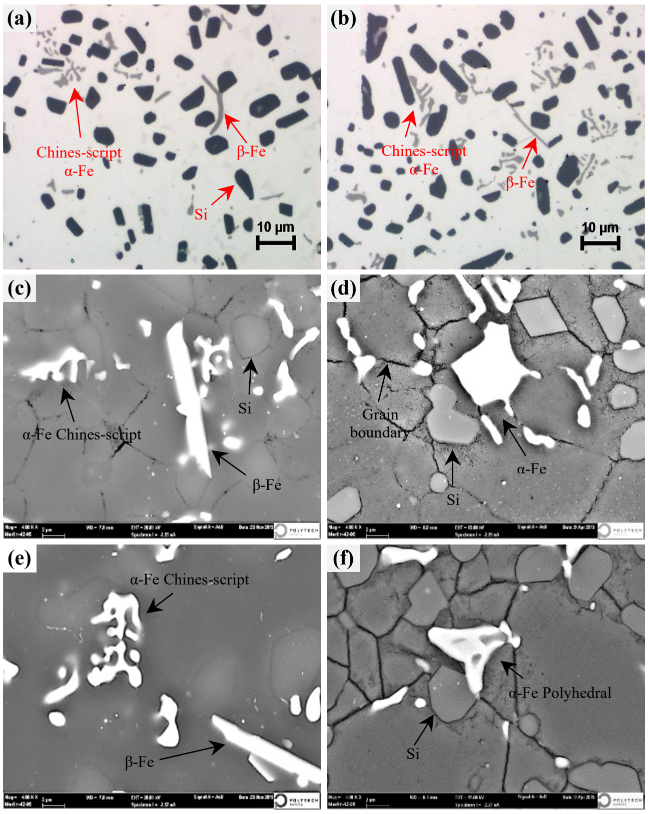

Figure 6. Micrographs of the $AlSi_{12}Cu$ alloy after solution heat treatment at 540°C (a-b), followed by aging at 180°C for (c) 4 h, (d) 8 h, and (e-f) 30 h. Images (a), (c), and (e) correspond to the SC, whereas images (b), (d), and (f) correspond to the HPDC.

3.3 Hardness test results

3.3.1 As-cast state

The superior mechanical properties of the HPDC alloy compared with those of the SC alloy are generally attributed to differences in the morphology and particle size of the eutectic silicon obtained during the solidification process. In the as-cast state, the average hardness, which is based on 15 measurement points, is 101 HV for the HPDC alloy and 89 HV for the SC alloy, with an error bar of approximately 3 HV in each case. The 13% increase in hardness of the HPDC alloy relative to the SC alloy is due to the high cooling rate during solidification, which transforms the large acicular silicon particles into a fine fibrous form.

3.3.2 Artificial aging

The addition of elements such as copper and magnesium can promote the precipitation of hardening phases, such as Al_2Cu and Mg_2Si, during artificial aging. These precipitates play crucial roles in strengthening the alloy by impeding dislocation movement, resulting in improvements in strength and hardness [17,21,22]. Figure 7 shows the variation in hardness as a function of aging time at 180°C for both the SC and HPDC alloys. Three hardness peaks were observed in both age-hardening curves. At the start of aging, the hardness increases with increasing aging time, reaching the first peak at approximately 20 min for HPDC and at 40 min for SC. Following these initial rapid peaks, the hardness decreases and then increases again, reaching a second peak at 4 h for HPDC and 8 h for SC. The final peaks are observed at 30 h for both the HPDC and SC alloys. After this peak, the hardness of the alloy decreases rapidly in both cases due to overaging.

The maximum hardness values occurred at the second peaks, at 4 h for HPDC and 8 h for SC alloys, with approximate measured values of 108 HV and 105 HV, respectively. The accelerated hardness peak observed at 4 h for HPDC, compared with 8 h for SC, is attributed to the higher pressure applied during solidification and the faster cooling rate, which promote the formation of nonequilibrium phases. These results are consistent with the work of Abou El-Khair [31], who demonstrated that increasing the squeeze pressure (from 70 MPa to 160 MPa) accelerates the alloy strength and reduces the time needed to reach the peak hardness from 8 h to 4 h.

3.4 X-ray diffraction analyses

XRD is a technique for measuring the arrangement and spacing of atoms in alloys. Heating or cooling, combined with pressure, leads to slight changes in the interplanar spacing, which generally results in slight changes in the angles of the diffraction peaks. In a previous study [3], a comparative analysis of the XRD patterns of both the as-cast SC and HPDC alloys revealed a slight angular shift of all the diffraction peaks. This phenomenon can be attributed to the macrostresses generated by the pressure during HPDC.

In this study, we compared the XRD patterns of SC and HPDC alloys after different aging times. Figure 8(a-b) present the XRD patterns of the SC and HPDC alloys at various aging durations, which are observed within the range of 20° to 120° (2θ). The magnified views of the Al (200) and Si (220) peaks in Figure 8(c-d) highlight shifts in the positions of the Bragg reflections. Compared with those of the other XRD peaks, all the XRD peaks corresponding to the aged peaks in the hardness curves (Figure 7) are shifted to the right. These peak shifts are observed at 20 min, 4 h, and 30 h in the SC alloy and at 40 min, 8 h, and 30 h in the HPDC alloy. The peak shifts in the SC alloy were more pronounced and more clearly distinguishable than those in the HPDC alloy. This difference is attributed to the slower solidification process in SC than in HPDC.

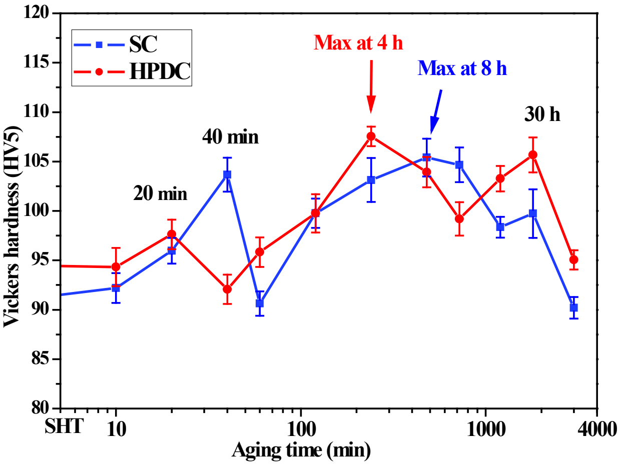

Figure 7. Hardness of the $AlSi_{12}Cu$ alloy produced by SC and HPDC after different aging times.

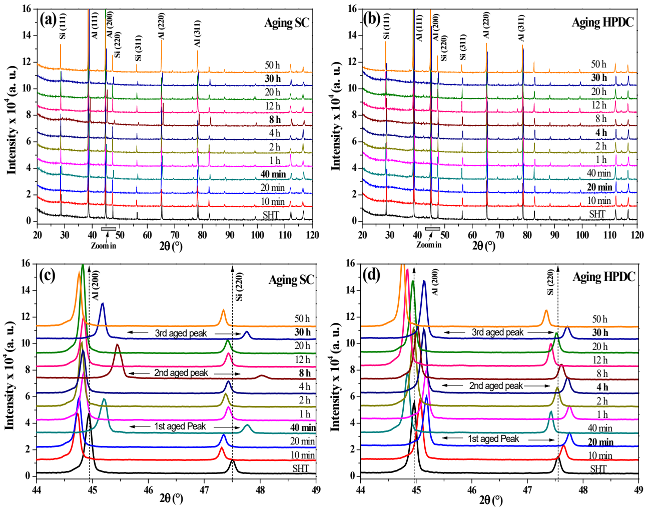

Figure 8. Superposition of normalized XRD patterns for SC and HPDC alloys at different aging times: (a) and (b). Corresponding enlarged views of the Al (200) and Si (220) diffraction peaks are shown in (c) and (d), respectively, highlighting microscopic elastic deformation.

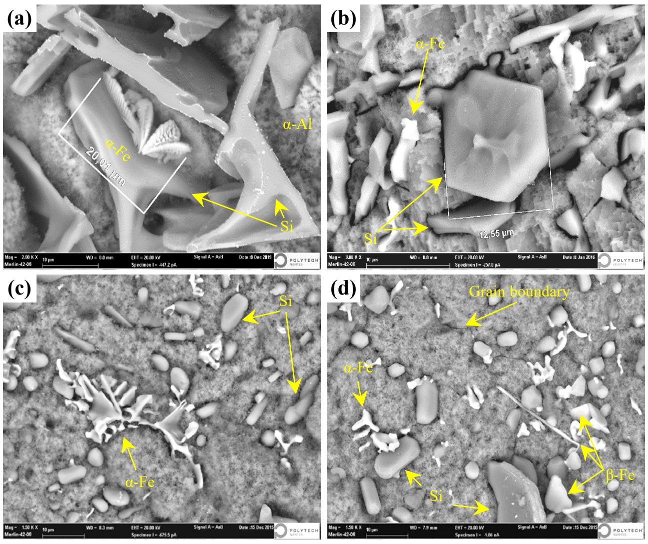

Figure 9. BSE micrographs of deep-etched alloys, illustrating their morphology before and after SHT: (a) and (c) for SC, and (b) and (d) for HPDC.

The broadening, along with the displacement of the diffraction angles of the aged peaks to the right, indicates the precipitation of hardening phases within the matrix. These phases introduce dislocations, leading to variations in the crystal lattice parameters. The changes in the shape of the diffraction peaks can be attributed to various microstructural factors, such as crystal disorientation, dislocation density, and phase precipitation resulting from heat treatments. As reported by Ji [32], the observed shift in the diffraction angle after heat treatment closely aligns with the evolution of hardness values.

3.5 Morphology of deep etching phases

In aluminum–silicon foundry alloys, the morphologies of silicon and intermetallic phases can differ significantly depending on the solidification conditions. The microstructures may experience notable transformations when transitioning from SC to HPDC processes. When observed in 3D, primary silicon is generally found in both casting processes as regular polyhedral particles or massive plate-like crystals. Figure 9(a) illustrates the eutectic silicon in the SC, which appears as large faceted silicon platelets. This figure shows the edges of some primary silicon platelets cut in cross-section and aligned parallel to the polishing plane of the sample. In the HPDC (Figure 9(b)), silicon appears as small, relatively smooth platelets with minimal traces of faceting. This figure also depicts primary silicon in the form of massive platelets, which exhibit an almost perfect hexagonal shape. Figure 9(a) also displays the α-Fe Chinese-script in 3D, showing a unique, interconnected, skeleton-like morphology. This phase, which crystallizes on the primary eutectic platelets and measures approximately 20 μm, is likely formed during the coeutectic or posteutectic stages of solidification. These intermetallics are more prevalent in SC and less common in HPDC, where they tend to precipitate into other intermetallics, such as α-Fe polyhedral particles.

After the SHT process, all intermetallic phases are dissolved except for the Fe-based intermetallics, as shown in Figure 9(c-d). The fragmentation, spheroidization, and dissolution of these phases are driven primarily by atomic diffusion movements [33]. A comparison of the silicon particles in the SC and HPDC alloys reveals that spheroidization and coalescence are less pronounced in the SC alloy than in the HPDC alloy (Figure 9(b)); this suggests that the fragmentation, coagulation, and spheroidization of eutectic silicon occur more rapidly in HPDC alloys than in SC alloys. According to the literature [34], a high cooling rate during the solidification process can significantly reduce the solution heat treatment time (SHT) by quickly altering the morphology of the eutectic silicon. As a result, disintegration, spheroidization, and coarsening of eutectic silicon progress faster in HPDC alloys than in SC alloys.

3.6 The Fe intermetallics in industrial $AlSi_{12}Cu$

The mechanical properties of $AlSi_{12}Cu$ alloys are strongly influenced by the morphology of their intermetallic phases. β-Fe intermetallics manifest as needle-like structures in two dimensions (2D) and platelets in three dimensions (3D). These phases are known to adversely affect mechanical properties due to their brittleness and stress concentration effects. These intermetallics also act as barriers to liquid metal flow during solidification, leading to the formation of pores in the microstructure. Roy *et al.* [35] reported that β-Fe particles serve as potential nucleation sites for porosity, regardless of the alloy composition or the size of the β-Fe particles. Figure 10(a) provides a clear example of how β-Fe platelets can act as barriers to liquid metal feeding in areas prone to shrinkage porosity. The presence of these intermetallics near the pores highlights their three-dimensional morphologies and lengths.

In the presence of Mn, Fe primarily crystallizes as the α-Fe Chinese-script phase at low to intermediate cooling rates. In ingot casting, where the cooling rate is lower than that in sand casting, the α-Fe Chinese-script phase becomes the dominant Fe intermetallic phase. Figure 10(c) shows that the α-Fe Chinese-script phase nucleates above the eutectic Si, confirming that this phase forms at the posteutectic stage. The bright spot on the Chinese-script α-Fe corresponds to Pb (lead), which appears brighter in the image due to it being a heavy element (high atomic number).

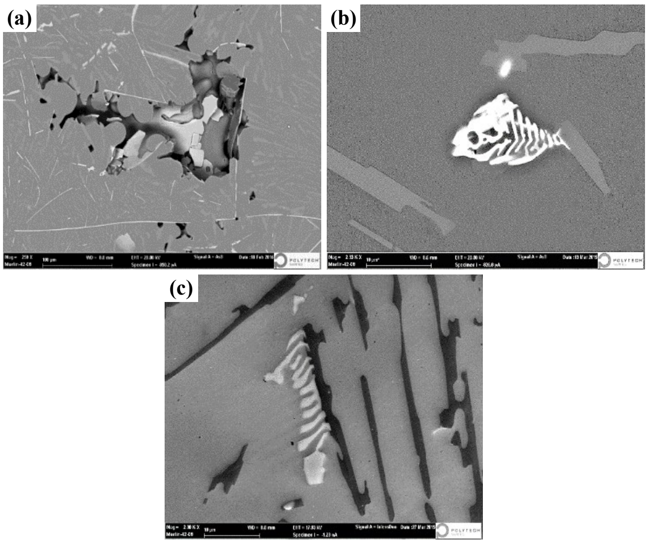

Figure 10. (a) and (b) Backscattered electron images showing β-Fe platelets in SC, with pores nucleating along their elongated sides, and the α-Fe Chinese-script phase in the ingot. (c) An InlensDuo image showing the transformation of primary polyhedral α-Fe into Chinese-script α-Fe, which nucleates on the eutectic Si phase.

Figure 10(d) presents an InlensDuo micrograph (BSE coupled with SE image), revealing the morphology and distribution of the α–Fe phase in the SC samples. The polyhedral α-Fe shown in this figure appears to be the source of growth for the branched arms of the α-Fe Chinese-script phase; it was likely formed at high temperatures during the predendritic phase of solidification. The growth of these branched arms seems to have started after the formation of the Si eutectic. It is also clear that the presence of arms of Chinese-script nucleated on the Si eutectic particles indicates that the eutectic Si particles arrived first and that the arms of the Chinese-script phase formed after the eutectic Si particles in the last posteutectic solidification stage [26].

4. Conclusions

From the effects of the casting process and aging treatment on the microstructure and hardness of the AlSi$_{12}$Cu cast alloys, the following conclusions can be drawn:

1. HPDC results in a more refined microstructure with a non-uniform distribution of primary α-Al dendrites due to nonequilibrium cooling. In contrast, SC leads to a coarser microstructure characterized by larger SDAS and coarse Si eutectic platelets owing to longer solidification times. The β-Fe platelets exhibit variations in both size and distribution, which are influenced mainly by cooling rate differences and the specific timing of their nucleation and growth during the solidification process. The α-Fe intermetallics formed two distinct phases: predominantly with a Chinese-script morphology in SC and as polyhedral particles in HPDC.
2. SHT at 540°C completely dissolves the θ-Al$_2$Cu, β-Mg$_2$Si, Q-Al$_5$Cu$_2$Mg$_8$Si$_6$ and π-Al$_8$Mg$_3$FeSi$_6$ phases, with the exception of the Fe-based intermetallics. The initial eutectic Si morphology in as-cast alloys differs between SC and HPDC, significantly influencing Si particle characteristics following heat treatment. Compared with SC alloys, HPDC alloys demonstrate higher coarsening rates of eutectic Si.
3. For both alloys, three hardness peaks were observed at 40 min, 8 h, and 30 h for the SC alloy, whereas for the HPDC alloy, they occurred at 20 min, 4 h, and 30 h. HPDC accelerates the hardness peak from 8 h to 4 h.
4. The shift of the diffraction peaks to the right in the XRD patterns of both alloys confirms a change in the lattice parameter of the matrix, which is attributed to the precipitation of hardening phases. The hardness and XRD results exhibit similar trends and are in good agreement, indicating that both analyses are consistent with each other.

Acknowledgments

The authors would like to thank Mr. Yazid Mahroug and Mr. Abdennour Yahyouche from the agricultural tractor company ETRAG in Constantine for their assistance in producing the foundry aluminum samples.

References

[1] *ASM Handbook Committee*, Materials Park, technical editor. ASM International, USA, Casting of Nonferrous Alloys, vol. 15. 2008. pp 1009-1018.

[2] A. M. A. Mohamed, A. M. Samuel, F. H. Samuel, and H. W. Doty, "Influence of additives on the microstructure and tensile properties of near-eutectic Al-10.8%Si cast alloy," *Materials and Design*, vol. 30, no. 10, pp. 3943-3957, 2009.

[3] S. Beroual, Z. Boumerzoug, P. Paillard, and Y. Borjon-piron, "Comparative study on the microstructures and hardness of the AlSi$_{10.6}$CuMg alloy produced by sand casting and high pressure die casting," *International Journal of Cast Metals Research,* vol. 00, no. 00, pp. 1-22, 2019.

[4] M. Okayasu, Y. Ohkura, S. Takeuchi, S. Takasu, H. Ohfuji, and T. Shiraishi, "A study of the mechanical properties of an Al-Si-Cu alloy (ADC12) produced by various casting processes," *Materials Science and Engineering A*, vol. 543, pp. 185-192, 2012.

[5] M. T. Murray, and M. Murray, "High pressure die casting of aluminium and its alloys", *Woodhead Publishing Limited*, vol. 1849. pp. 217-261, 2011.

[6] O. El Sebaie, A. M. Samuel, F. H. Samuel, and H. W. Doty, "The effects of mischmetal, cooling rate and heat treatment on the hardness of A319.1, A356.2 and A413.1 Al-Si casting alloys," *Materials Science and Engineering A*, vol. 486, no. 1-2, pp. 241-252, 2008.

[7] C. L. Yang, Y. B. Li, B. Dang, H. Bin Lü, and F. Liu, "Effects of cooling rate on solution heat treatment of as-cast A356 alloy," *Transactions of Nonferrous Metals Society of China (English Edition)*, vol. 25, no. 10, pp. 3189-3196, 2015.

[8] C. Chanmuang, W. Kongmuang, J. Pearce, and T. Chairuangsri, "Influence of casting techniques on hardness, tarnish behavior and microstructure of Ag-Cu-Zn-Si sterling silver jewelry alloys," *Journal of Metals, Materials and Minerals*, vol. 22, no. 2, pp. 19-26, 2012.

[9] S. G. Shabestari, and H. Moemeni, "Effect of copper and solidification conditions on the microstructure and mechanical properties of Al–Si–Mg alloys," *Journal of Materials Processing Technology,* vol. 154, pp. 193-198, 2004.

[10] F. H. Samuel, A. M. Samuel, and H. Liu, "Effect of magnesium content on the ageing behaviour of water-chilled Al-Si-Cu-Mg-Fe-Mn (380) alloy castings," *Journal of Materials Science*, vol. 30, no. 10, pp. 2531-2540, 1995.

[11] S. Shankar, and D. Apelian, "Die soldering: Mechanism of the interface reaction between molten aluminum alloy and tool steel," *Metallurgical and Materials Transactions B*, vol. 33, no. 3, pp. 465–476, 2002.

[12] L. F. Mondolfo. *Aluminum alloys: structure and properties*. London and Boston, Butterworth; 1976.

[13] D. Apelian, and M. Makhlouf, "Casting Characteristics of Aluminum Die Casting Alloys," *FINAL REPORT*, pp. 1-46, 2002.

[14] S. A. Kori, M. S. Prabhudev, and T. M. Chandrashekharaiah, "Studies on the microstructure and mechanical properties of A356 alloy with minor additions of copper and magnesium," *Transactions of the Indian Institute of Metals*, vol. 62, no. October, pp. 353-356, 2009.

[15] I. Alfonso, C. Maldonado, G. Gonzalez, and A. Bedolla, "Effect of Mg content and solution treatment on the microstructure of Al-Si-Cu-Mg alloys," *Journal of Materials Science*, vol. 41, no. 7, pp. 1945-1952, 2006.

[16] J. A. Taylor, D. H. St John, J. Barresi, and M. J. Couper, "Influence of Mg content on the microstructure and solid solution chemistry of Al-7%Si-Mg casting alloys during solution treatment," *Materials Science Forum*, vol. 331, pp. 277-282, 2000.

[17] S. Shivkumar, S. Ricci, C. Keller, and D. Apelian, "Effect of solution treatment parameters on tensile properties of cast aluminum alloys," *Journal of Heat Treating*, vol. 8, no. 1, pp. 63-70, 1990.

[18] M. Samoshina, and N. Belov, "The features of phase composition and microstructure of eutectic piston alloys $AlSi_{12}CuMgNi$ and $AlSi_{12}Cu_2MgNi$. In: Weiland, H., Rol-lett, A.D., Cassada, W. A. (eds) *ICAA13* Pittsburgh: Proceedings of the *13th International Conference on Aluminum Alloys*. Springer, Cham, pp. 1245-1250, 2012.

[19] E. Sjölander, and S. Seifeddine, "The heat treatment of Al-Si-Cu-Mg casting alloys," *ournal of Materials Processing Technology*, vol. 210, no. 10, pp. 1249-1259, 2010.

[20] P. Ouellet, and F. H. Samuel, "Effect of Mg on the ageing behaviour of Al-Si-Cu 319 type aluminium casting alloys," *Journal of Materials Science*, vol. 34, pp. 4671-4697, 1999.

[21] R. X. Li, R. D. Li, Y. H. Zhao, L. Z. He, C. X. Li, H. R. Guan, and Z. Q. Hu "Age-hardening behavior of cast Al-Si base alloy," *Materials Letters*, vol. 58, no. 15, pp. 2096-2101, 2004.

[22] X. Dong, S. Amirkhanlou, and S. Ji, "Formation of strength platform in cast Al-Si-Mg-Cu alloys," *Scientific Reports*, vol. 9, no. 1, pp. 1-11, 2019.

[23] Material Properties Database, [Online]. Available: http://www.makeitfrom.com/material-properties/413.0-413.0-F-S12B-A04130-Cast-Aluminum

[24] C. M. Gourlay, H. I. Laukli, and A. K. Dahle, "Defect band characteristics in Mg-Al and Al-Si high-pressure die castings," *Metallurgical and Materials Transactions A*, vol. 38, no. 8, pp. 1833-1844, 2007.

[25] G. Timelli, A. Fabrizi, S. Capuzzi, F. Bonollo, and S. Ferraro, "The role of Cr additions and Fe-rich compounds on microstructural features and impact toughness of $AlSi_9Cu_3$(Fe) diecasting alloys," *Materials Science and Engineering A*, vol. 603, pp. 58-68, 2014.

[26] X. Cao, and J. Campbell, "The solidification characteristics of Fe-rich intermetallics in Al-11.5Si-0.4Mg cast alloys," *Metallurgical and Materials Transactions A*, vol. 35 A, no. 5, pp. 1425-1435, 2004.

[27] S. G. Shabestari, and S. Ghodrat, "Assessment of modification and formation of intermetallic compounds in aluminum alloy using thermal analysis," *Materials Science and Engineering A*, vol. 467, no. 1-2, pp. 150-158, 2007.

[28] S. Seifeddine, E. Sjölander, and T. Bogdanoff, "On the role of copper and cooling rates on the microstructure, defect formations and mechanical properties of Al-Si-Mg alloys," *Materials Sciences and Applications*, vol. 04, no. 03, pp. 171-178, 2013.

[29] S. Beroual, Z. Boumerzoug, P. Paillard, and Y. Borjon-piron, "Effects of heat treatment and addition of small amounts of Cu and Mg on the microstructure and mechanical properties of Al-Si-Cu and Al- Si-Mg cast alloys," *Journal of Alloys and Compounds*, vol. 784, pp. 1026-1035, 2019.

[30] E. Tillova, M. Chalupova, and L. Hurtalova, "Evolution of the Fe-rich phases in recycled $AlSi_9Cu_3$ cast alloy during solution treatment," *Journal Communications - Scientific Letters of the University of Žilina*, vol. 12, no. 4, pp. 95-101, 2010.

[31] M. T. A. El-khair, "Microstructure characterization and tensile properties of squeeze-cast AlSiMg alloys," *Materials Letters*, vol. 59, pp. 894-900, 2005.

[32] V. Ji, "Contribution à l'analyse par diffraction des rayons X de l'état microstructural et mécanique des matériaux hétérogènes (Contribution to X-ray diffraction analysis of the microstructural and mechanical state of heterogeneous materials), Thesis, Lille University, France, 2004.

[33] Y. Du, Y.A. Chang, B. Huang, W. Gong, Z. Jin, H. Xu, Z. Yuan, Y. Liu, Y. He, and F.Y. Xie, "Diffusion coefficients of some solutes in fcc and liquid Al: Critical evaluation and correlation," *Materials Science and Engineering A*, vol 363, pp 140-151, 2003

[34] C. L. Yang, Y. B. Li, B. Dang, H. Bin Lü, and F. Liu, "Effects of cooling rate on solution heat treatment of as-cast A356 alloy," *Transactions of Nonferrous Metals Society of China,* vol. 25, no. 10, pp. 3189-3196, 2015.

[35] N. Roy, A. M. Samuel, and F. H. Samuel, "Porosity formation in AI-9 Wt Pet Si-3 Wt Pet Cu alloy systems: Metallographic observations," *Metallurgical and Materials Transactions A*, vol. 27, no. 2, pp. 415-429, 1996.